



# Fast Radio Bursts from Activity of Neutron Stars Newborn in BNS Mergers: Offset, Birth Rate, and Observational Properties

F. Y. Wang<sup>1,2</sup> , Y. Y. Wang<sup>1</sup>, Yuan-Pei Yang<sup>3</sup> , Y. W. Yu<sup>4</sup>, Z. Y. Zuo<sup>5</sup>, and Z. G. Dai<sup>1,2</sup>

<sup>1</sup> School of Astronomy and Space Science, Nanjing University, Nanjing 210093, People's Republic of China; [fayinwang@nju.edu.cn](mailto:fayinwang@nju.edu.cn)

<sup>2</sup> Key Laboratory of Modern Astronomy and Astrophysics (Nanjing University), Ministry of Education, Nanjing 210093, People's Republic of China

<sup>3</sup> South-Western Institute for Astronomy Research, Yunnan University, Kunming, People's Republic of China; [ypyang@ynu.edu.cn](mailto:ypyang@ynu.edu.cn)

<sup>4</sup> Institute of Astrophysics, Central China Normal University, Wuhan 430079, People's Republic of China

<sup>5</sup> School of Science, Xi'an Jiaotong University, Xi'an, 710049, People's Republic of China

Received 2019 September 2; revised 2020 February 6; accepted 2020 February 9; published 2020 March 5

## Abstract

Young neutron stars (NSs) born in core-collapse explosions are promising candidates for the central engines of fast radio bursts (FRBs), since the first localized repeating burst FRB 121102 occurs in a star-forming dwarf galaxy similar to the host galaxies of superluminous supernovae and long gamma-ray bursts. However, FRB 180924 and FRB 190523 are localized to massive galaxies with low rates of star formation, compared with the host of FRB 121102. The offsets between the bursts and host centers are about 4 and 29 kpc for FRB 180924 and FRB 190523, respectively. These host properties are similar to those of short gamma-ray bursts (GRBs), which are produced by binary neutron star (BNS) or NS–black hole mergers. Therefore, the NSs powering FRBs may be formed in BNS mergers. In this paper, we study BNS merger rates and merger times, and predict the most likely merger locations for different types of host galaxies using the population synthesis method. We find that the BNS merger channel is consistent with the recently reported offsets of FRB 180924 and FRB 190523. The offset distribution of short GRBs is well reproduced by population synthesis using a galaxy model similar to that of GRB hosts. The event rate of FRBs (including non-repeating and repeating), is larger than those of BNS mergers and short GRBs, and requires a large fraction of observed FRBs emitting several bursts. Using curvature radiation by bunches in NS magnetospheres, we also predict the observational properties of FRBs from BNS mergers, including the dispersion measure and rotation measure. At late times ( $t \geq 1$  yr), the contribution to dispersion measure and rotation measure from BNS merger ejecta can be neglected.

*Unified Astronomy Thesaurus concepts:* Radio bursts (1339); Gamma-ray bursts (629); Magnetars (992); Binary stars (154); Gravitational waves (678)

## 1. Introduction

Fast radio bursts (FRBs) are transients of coherent emission lasting about a few milliseconds (Lorimer et al. 2007; Thornton et al. 2013; Champion et al. 2016; Shannon et al. 2018; Cordes & Chatterjee 2019; Platts et al. 2019; Petroff et al. 2019) with large dispersion measures (DMs). Thanks to multi-wavelength follow-up observations and precise localization, the repeating FRB 121102 was localized in a dwarf star-forming galaxy at  $z = 0.19$  (Chatterjee et al. 2017; Marcote et al. 2017; Tendulkar et al. 2017). This FRB is also spatially associated with a persistent radio source (Chatterjee et al. 2017; Marcote et al. 2017). The properties of this galaxy are similar to those of host galaxies of superluminous supernovae (SLSNe) and long gamma-ray bursts (GRBs; Metzger et al. 2017; Nicholl et al. 2017; Tendulkar et al. 2017; Zhang & Wang 2019). This has led to the hypothesis that bursts are produced by young active neutron stars (NSs; Popov & Postnov 2013; Kulkarni et al. 2014; Lyubarsky 2014; Katz 2016b; Lu & Kumar 2016; Murase et al. 2016; Beloborodov 2017, 2019; Wang & Yu 2017; Metzger et al. 2017; Lu & Kumar 2018; Yang & Zhang 2018; Wang & Lai 2019; Cheng et al. 2020). The young active NSs are born in core-collapse explosions. Recently, a second repeating FRB, 180916.J0158+65, was localized to a star-forming region in a nearby massive spiral galaxy (Marcote et al. 2020). Two coherent mechanisms are often considered in current FRB models: curvature radiation by bunches (Katz 2014, 2018a; Kumar et al. 2017; Ghisellini & Locatelli 2018; Yang & Zhang 2018) and maser mechanisms (Lyubarsky 2014;

Beloborodov 2017; Ghisellini 2017; Waxman 2017; Lu & Kumar 2018; Beloborodov 2019; Metzger et al. 2019).

Recently, two FRBs, which are both single bursts, have been localized to massive galaxies by the Australian Square Kilometre Array Pathfinder and Deep Synoptic Array ten-antenna prototype (DSA-10) respectively. FRB 180924 occurred in a massive galaxy at redshift  $z = 0.32$  with lower star formation rate (Bannister et al. 2019). The offset between the burst and host galaxy center is about 4 kpc (Bannister et al. 2019). The DM contributed by the host galaxy of FRB 180924 is small (between 30 and 81  $\text{pc cm}^{-3}$ ), allowing FRBs to be a promising cosmological probe (Gao et al. 2014; Zhou et al. 2014; Wei et al. 2015; Yang & Zhang 2016; Yu & Wang 2017, 2018; Li et al. 2018, 2019b; Liu et al. 2019; Walters et al. 2018; Wang & Wang 2018; Zhang 2018a). DSA-10 localized FRB 190523 to a massive galaxy at a redshift of 0.66 (Ravi et al. 2019). This galaxy is different from the host of FRB 121102, as it is about a thousand times more massive, with a specific star formation rate two orders of magnitude lower (Ravi et al. 2019). Aside from the two confirmed host galaxies, Li et al. (2019a) recently found that the host candidates of some nearby FRBs are also dissimilar to that of FRB 121102. This low star formation rate and large offset of FRB hosts indicate that the NSs powering FRBs may be formed by mergers of binary neutron stars (BNSs), which are similar to short GRBs. Observationally, short GRBs occur in early-type galaxies with low star formation (Barthelmy et al. 2005; Gehrels et al. 2005; Bloom et al. 2006) and have large offsets from the centers of the host galaxies (Fox et al. 2005;

Fong et al. 2013). Some short GRBs show X-ray flares and internal plateaus with rapid decay at the end of the plateaus, consistent with a millisecond NS born in a BNS merger (Dai et al. 2006; Metzger et al. 2008; Rowlinson et al. 2013; Wang & Dai 2013; Lü et al. 2015; Gao et al. 2016; Ai et al. 2019).

There are at least two distinct NS formation channels, i.e., core-collapse explosions and BNS mergers. The BNS merger channel is different from the core-collapse explosion channel in two aspects. First, the ejecta produced by BNS mergers has higher velocity ( $v \sim (0.1-0.3) c$ ) and lower mass ( $(10^{-4} - 10^{-2})M_{\odot}$ ), compared with those of core-collapse explosion. The ejecta can affect the observational properties of FRBs (Margalit et al. 2019). Second, the offsets in the two cases are different. At the time of birth, NSs receive natal kicks, which are connected to asymmetries in supernova explosions. Due to the long delay time, BNSs will merge at large radius in host galaxies even if born at small radius (Bloom et al. 1999; Fryer et al. 1999; Belczynski et al. 2006). However, in our population synthesis, most primary neutron stars receive small kicks (see Section 2.6 for details). Margalit et al. (2019) also studied the properties of FRBs from magnetars born in BNS mergers and accretion-induced collapse.

In this paper, we undertake an updated analysis of BNS mergers using population synthesis methods (Bloom et al. 1999; Fryer et al. 1999; Belczynski et al. 2002, 2006; Perna & Belczynski 2002; Voss & Tauris 2003) and calculate the FRB properties from BNS mergers. Compared with previous population synthesis codes (Hurley et al. 2002; Belczynski et al. 2008), the new version of the binary star evolution (BSE) code (Banerjee et al. 2019) includes several major upgrades. The most important one is the new formation channel of NSs from electron-capture supernovae (ECSs). For close binaries, stars with masses between 6 and 8  $M_{\odot}$  can form ECS-NSs (Podsiadlowski et al. 2004). We also show the properties of FRBs powered by NSs from BNS mergers using curvature radiation by bunches (Yang & Zhang 2018).

The paper is structured as follows. The description of the BSE code, galaxy potential models, and kick velocity are presented in Section 2. The results of population synthesis, including merger time and delay time distributions, offset distribution, and merger rate, are given in Section 3. In Section 4, we compare the event rates of FRBs, short GRBs, and BNS mergers. The observational properties of FRBs from NSs formed by BNS mergers are given in Section 5. Conclusions and a discussion are given in Section 6.

## 2. Compact Binaries from Population Synthesis

### 2.1. The BSE Code

The BSE code, developed by Jarrod Hurley, Onno Pols, and Christopher Tout, is a rapid binary-evolution algorithm based on a suite of analytical formulae (Hurley et al. 2002). It is incorporated into the  $N$ -body evolution program NBODY7 (Aarseth 2012) for globular clusters as the stellar-evolutionary sector. Three major upgrades are added to the new version of the BSE code (Banerjee et al. 2019): (i) semi-empirical stellar wind prescriptions (Belczynski et al. 2010), (ii) remnant formation and material fallback (Fryer et al. 2012) and the occurrences of pair-instability supernovae (PSNe) and pulsation pair-instability supernovae (PPSNe; Belczynski et al. 2016), and (iii) a modulation of the BHs' and the NSs' natal

kicks based on the fallback fraction during their formation (Banerjee et al. 2019).

The new BSE code includes the ECS-NS formation channel (Podsiadlowski et al. 2004; Belczynski et al. 2008) unlike the previous version (Hurley et al. 2002). The primary star in a binary system with initial mass in the range 6–8  $M_{\odot}$  is likely to become an ECS (Podsiadlowski et al. 2004), producing the ECS-NS, which typically has so small ( $<20 \text{ km s}^{-1}$ ) or zero kick velocity that it remains bound to globular clusters whose escape velocities are 10–20  $\text{km s}^{-1}$  (Katz 1975). These NSs are distinctly the least massive, born with characteristic mass  $m_{\text{ECS,NS}} = 1.26M_{\odot}$  (Banerjee et al. 2019).

We adopt the remnant-mass prescription of Belczynski et al. (2002) (`nsflag` = 1), no PPSN/PSN mass cutoff (`psflag` = 0), and standard momentum-conserving kick of Belczynski et al. (2008) (`kmech` = 1). The program `popbin` is used to carry out the population synthesis.

### 2.2. Parameter Distribution

We created a catalog of 1000,000 binary systems in which the the initial system parameters ( $M_1$ ,  $q$ ,  $e$ ,  $P$ ) satisfy the following distributions:

$$f_{M_1}(M_1) \propto M_1^{-\alpha}, \quad \text{for } M_1 \in [5, 100] \quad (1)$$

$$f_q(q) \propto q^{\kappa}, \quad \text{for } q \in [0.1, 1] \quad (2)$$

$$f_e(e) \propto e^{\eta}, \quad \text{for } e \in [0.0, 1.0] \quad (3)$$

$$f_P(\log_{10} P) \propto (\log_{10} P)^{\pi}, \quad \text{for } \log_{10} P \in [0.15, 5.5] \quad (4)$$

where  $M_1$  is the mass of the primary star,  $\alpha = 2.7$  (Scalo 1986),  $q \equiv m_2/m_1$  is the mass ratio of the two stars,  $P$  and  $e$  are orbital period and eccentricity respectively, and  $\kappa = 0$  (Bethe & Brown 1998),  $\eta = 1$  (Duquennoy & Mayor 1991), and  $\pi = 0.5$  (Sana et al. 2012) are used in our simulation. It is worth mentioning that the initial binary properties do not significantly affect (within a factor of 2) the predictions of double-compact object merger rates (de Mink & Belczynski 2015). The metallicity  $Z$  and maximum evolution time  $T$  are set to 0.02 and 15,000 Myr for all binaries.

### 2.3. Motion of Binaries in the Gravitational Field of the Galaxy

To obtain the predicted offset of the binary compact objects merger, we need to know the motion of the binary, which depends on its initial location and velocity, the gravitational field of the galaxy, the kick velocity, as well as the delay time. Here, we consider a spiral galaxy and elliptical galaxy of different sizes.

For a spiral galaxy, there are three components: a disk, a bulge, and a halo. The galactic disk and bulge potential was proposed by Miyamoto & Nagai (1975) as

$$\Phi_i(R, z) = -\frac{GM_i}{\sqrt{R^2 + (a_i + \sqrt{z^2 + b_i^2})^2}}, \quad (5)$$

where  $\Phi_1$  and  $\Phi_2$  refer to the bulge and disk potential respectively. The bulge potential  $\Phi_1$  is described by  $M_1 = 1.0 \times 10^{10}M_{\odot}$ ,  $a_1 = 0$ , and  $b_1 = 0.267 \text{ kpc}$ ; the disk potential  $\Phi_2$  is described by  $M_2 = 6.5 \times 10^{10}M_{\odot}$ ,  $a_2 = 4.4 \text{ kpc}$ , and  $b_2 = 0.308 \text{ kpc}$  (Bajkova & Bobylev 2017).

For an elliptical galaxy, only bulge and halo are considered. The bulge potential model is the Hernquist (1990) model:

$$\Phi(r) = -\frac{GM_e}{r + a_e}, \quad (6)$$

where  $M_e = 5 \times 10^{11} M_\odot$  and  $a_e = 5$  kpc (Belczynski et al. 2006).

The halo potential for both the spiral and elliptical galaxies is given by the Navarro–Frenk–White profile (Navarro et al. 1996)

$$\Phi_h(r) = -\frac{GM_h}{r} \ln\left(1 + \frac{r}{a_h}\right), \quad (7)$$

where  $M_h = 2.9 \times 10^{11} M_\odot$  and  $a_h = 7.7$  kpc are provided by Bajkova & Bobylev (2017).

#### 2.4. Initial Conditions

The cylindrical coordinates ( $R_0, z_0$ ) of the initial location of the binary obey the following distributions:

$$p_R(R) \propto R e^{-R/R_{\text{exp}}}, \quad (8)$$

$$p_z(z) \propto e^{-|z|/z_{\text{exp}}}, \quad (9)$$

where  $R_{\text{exp}} = 4.5$  kpc,  $R_{\text{max}} = 20$  kpc,  $z_{\text{exp}} = 75$  pc, and  $z_{\text{max}} = 300$  pc are used (Paczynski 1990). For a galaxy of different size, a scale factor  $\alpha$  is used to change the mass and spatial size proportionally, i.e.,  $M' = \alpha M$ ,  $R' = \alpha^{1/3} R$  (Belczynski et al. 2002), where  $M$  and  $R$  are the typical mass and spatial size of a Milky Way-like galaxy. In this study,  $\alpha = 1, 0.1, 0.01, 0.001$  are considered.

The initial velocity  $v_0$  is the local rotational velocity of the galaxy which has no vertical component (Belczynski et al. 2002):

$$v_0 = v_\phi(R) = \sqrt{\frac{GM(<R)}{R}} \quad (10)$$

where  $M(<R) = \int_{-\infty}^{+\infty} \int_0^R 2\pi R \rho(R, z) dR dz$  is the total mass within a cylinder of radius  $R$ ,  $\rho(R, z)$  is the density of the galaxy as a function of  $R$  and  $z$ .

#### 2.5. Equations of Motion

The binary's motion trajectory in the galactic potential field  $\phi$  can be obtained by solving the following equations:

$$\begin{aligned} \frac{dx}{dt} &= v_x, & \frac{dy}{dt} &= v_y, & \frac{dz}{dt} &= v_z, \\ \frac{dv_x}{dt} &= -\left(\frac{\partial\phi}{\partial x}\right)_{y,z}, \\ \frac{dv_y}{dt} &= -\left(\frac{\partial\phi}{\partial y}\right)_{x,z}, \\ \frac{dv_z}{dt} &= -\left(\frac{\partial\phi}{\partial z}\right)_{x,y} \end{aligned} \quad (11)$$

where  $x_0, y_0, v_{x0}, v_{y0}$  are obtained by projecting  $R_0$  and  $v_0$  into the  $x$  and  $y$  directions

$$x_0 = R_0 \cos(l_{\text{bin}}), \quad y_0 = R_0 \sin(l_{\text{bin}}) \quad (12)$$

$$v_{x0} = v_0 \cos\left(l_{\text{bin}} + \frac{\pi}{2}\right), \quad v_{y0} = v_0 \sin\left(l_{\text{bin}} + \frac{\pi}{2}\right) \quad (13)$$

where  $l_{\text{bin}}$  is the randomly sampled galactic longitude of the binary system. These six motion equations are different from those in cylindrical coordinates proposed by Paczynski (1990), in which the signs of  $\Phi_i(R, z)$ ,  $\left(\frac{\partial\Phi}{\partial R}\right)_z$  and  $\left(\frac{\partial\Phi}{\partial z}\right)_R$  are wrong. Solving the equations in a Cartesian coordinate system can avoid the difficulty of treating the signs of  $R$  and  $v_R$  signs when binaries move across the galactic center.

#### 2.6. Kick Velocities

NSs formed without any fallback receive full natal kicks,  $V_{\text{kick}}$ , which follow a Maxwellian distribution with dispersion  $\sigma = 190$  km s<sup>-1</sup> (Hansen & Phinney 1997; Hurley et al. 2002):

$$f(v) \propto \frac{v^2 e^{-v^2/(2\sigma^2)}}{\sigma^3}. \quad (14)$$

In the code model of the partial fallback case, the kick velocity  $v_{\text{kick}}$  is modified by the factor  $(1 - f_{\text{fb}})$ :

$$v_{\text{kick}} = V_{\text{kick}}(1 - f_{\text{fb}}), \quad (15)$$

where  $f_{\text{fb}}$  is the fraction of the stellar envelope that falls back. It is worth mentioning that this does not apply to all NSs. For ECS–NSs, the natal kicks follow a Maxwellian distribution with a small dispersion and are exempted from the fallback treatment (Banerjee et al. 2019). We assume the kick velocity of the second NS follows a Maxwellian distribution with  $\sigma = 190$  km s<sup>-1</sup> and the direction is perpendicular to the binary's velocity before the kick. Velocity additions are conducted to get the new velocities after the first kick and the second kick respectively. Then the motion of the binary can be divided into three parts by the time of first kick and the second kick. Each new velocity is used as the initial velocity for the next stage of motion to calculate the final offset.

### 3. Results of Population Synthesis

From the population synthesis, we obtain 5531 NS–NS mergers out of 10,000,000 binaries. For NS–NS systems, about 60 ~ 70% of the first NSs are ECS–NSs, which have zero or low kick velocities (~few km s<sup>-1</sup>). It is worth mentioning that we consider NS–NS systems that can give birth to stable NSs, which are possible FRB progenitors (Popov & Postnov 2013; Kulkarni et al. 2014; Lyubarsky 2014; Katz 2016b; Beloborodov 2017; Metzger et al. 2017; Lu & Kumar 2018; Yang & Zhang 2018). The maximum mass of the NS depends on the equation of state and spin period, which are still uncertain. We choose an rough upper limit as  $m_1 + m_2 \leq 2.6M_\odot$  or  $3M_\odot$ . We find 297 and 4523 possible NSs for the  $m_1 + m_2 \leq 2.6M_\odot$  and  $3M_\odot$  before merger respectively.

#### 3.1. Merger Time and Delay Time Distributions

The delay time is defined as the time between the birth of the binary system and the final merger, while merger time refers to the time interval between the binary compact object formation and the merger. In Figure 1, we show the delay time distribution and merger time distribution for NS–NS binaries. The merger times of eight observed field Galactic NS–NS systems

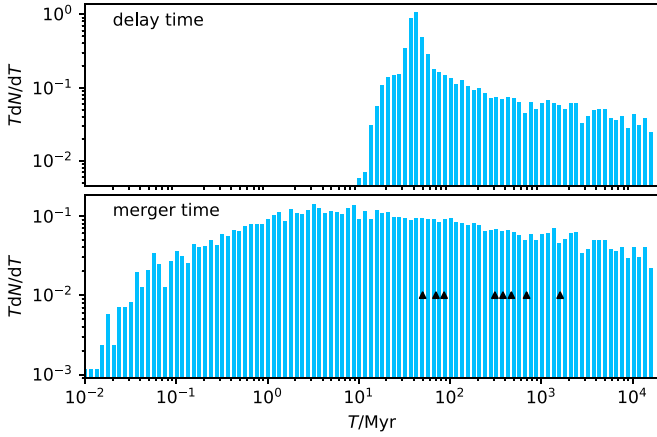


**Figure 1.** Merger time and delay time distributions for NS–NS systems. The eight Galactic NS–NS systems are shown as triangles.

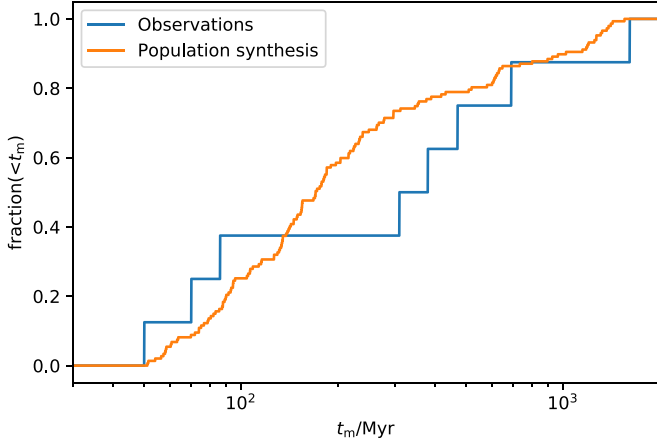


**Figure 2.** Cumulative distribution of merger times for NS–NS from population synthesis (orange) and observations (blue). The  $p$  value is 0.22 from the Kolmogorov–Smirnov test.

(Beniamini & Piran 2019) are shown as triangles. We also compare the cumulative distributions of merger time from population synthesis with these eight observed field Galactic NS–NS systems. The result is shown in Figure 2. From the Kolmogorov–Smirnov test, the  $p$  value is 0.22, which supports that they follow the same distribution. For the delay time, as NSs’ progenitors are massive stars, their birth rate follows the star formation rate (SFR) with a minimal delay. The delay time is dominated by this gravitational wave (GW) inspiral time. The time until merger depends on the initial semimajor axis  $a$ , and the eccentricity  $e$  of the BNS as  $t_m \propto a^4(1-e)^{7/2}$ . Under some assumptions, the delay time distribution is  $dN/dt \propto t^{-1}$  at late times ( $t \geq 1$  Gyr) (Piran 1992; Totani et al. 2008). From Figure 1, it is obvious that the merger times from population synthesis show a similar distribution. Figure 3 shows the merger time and delay time distributions for NS–NS mergers that may produce stable NSs. We can see that the distributions of delay time and merger time are almost the same in Figures 1 and 3.

### 3.2. Offset Cumulative Distribution

The cumulative distributions of offsets between merger locations and centers of host galaxies for NS–NS mergers are shown in Figures 4 and 5 for spiral galaxies and elliptical galaxies, respectively. The projected offset is the offset in the

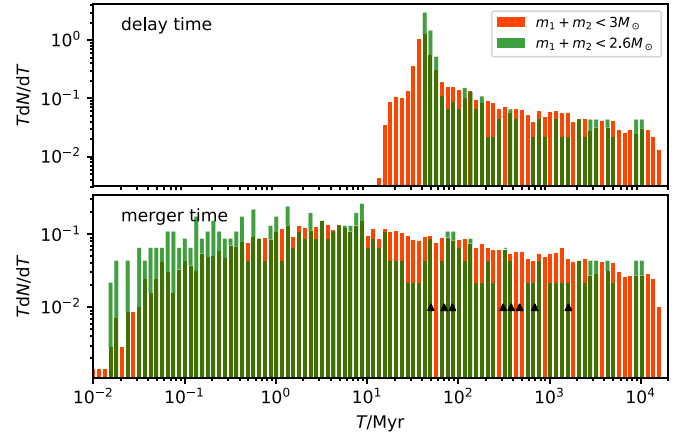


**Figure 3.** Merger time and delay time distribution for NS–NS systems whose mergers may produce stable NSs.

direction perpendicular to the line of sight. In the calculations, we average over all possible orientations of host galaxies. The observed offsets of GW170817/GRB 170817A (2 kpc) (Levan et al. 2017), FRB 180924 (4 kpc) (Bannister et al. 2019), FRB 180916 (4.7 kpc) (Marcote et al. 2020), and FRB 190523 (29 kpc) (Ravi et al. 2019), and offsets distribution of short GRBs (Fong et al. 2010, 2013; Berger 2014) are also shown for comparison. For massive spiral galaxies ( $\alpha = 1$ ), 60% of NS–NS systems will have offsets larger than 10 kpc, while for low-mass spiral galaxies ( $\alpha = 0.001, 0.01, 0.1$ ), the fraction is about 30%. For elliptical galaxies, the cumulative distributions of offsets are steeper when galaxy mass increases. For massive elliptical galaxies ( $\alpha = 0.1, 1$ ) in Figure 5, the observed offsets of short GRBs are consistent with simulated NS–NS systems. The observed median mass of short GRBs host galaxies is about  $10^{10} M_\odot$  (Berger 2014), which corresponds to the  $\alpha = 0.1$  case.

Figures 6 and 7 show the offset distributions for NS–NS mergers that may produce NSs in spiral and elliptical galaxies respectively. For massive galaxies, the offset distributions for different upper limits of newborn NSs are almost the same. For low-mass galaxies ( $10^8 M_\odot$ ), about 70% of NS–NS systems will merge with offsets less than 5 kpc for  $m_1 + m_2 \leq 3.0 M_\odot$  case, while it is more than 80% for the  $m_1 + m_2 \leq 2.6 M_\odot$  case.

### 3.3. Merger Rate

The merger rate  $R_m(z)$  is a convolution of the SFR history  $\rho(z)$  and the probability density function of delay time

$$R_m(z) = \int_{t(z)}^{t(z=\infty)} f\rho(z)(t')p[t(z) - t']dt', \quad (16)$$

where  $dt = -H(z)^{-1}(1+z)^{-1}dz$ ,  $H(z)$  is the Hubble parameter as a function of  $z$ ,  $f$  is the mass fraction of the compact binaries (NS–NS) to the entire stellar population, and  $t(z)$  is the cosmic age at redshift  $z$ . The cosmic star formation rate is taken from Madau & Dickinson (2014):

$$\rho(z) = 0.015 \frac{(1+z)^{2.7}}{1 + [(1+z)/2.9]^{5.6}} M_\odot \text{yr}^{-1} \text{Mpc}^{-3}. \quad (17)$$

When calculating the integration, we ignore the factor  $f$ , just showing the shape of the merger rate as a function of redshift. The merger rates  $R_m(z)$  as a function of redshift  $z$  are plotted in Figure 8 for  $m_1 + m_2 \leq 3 M_\odot$  before merger.

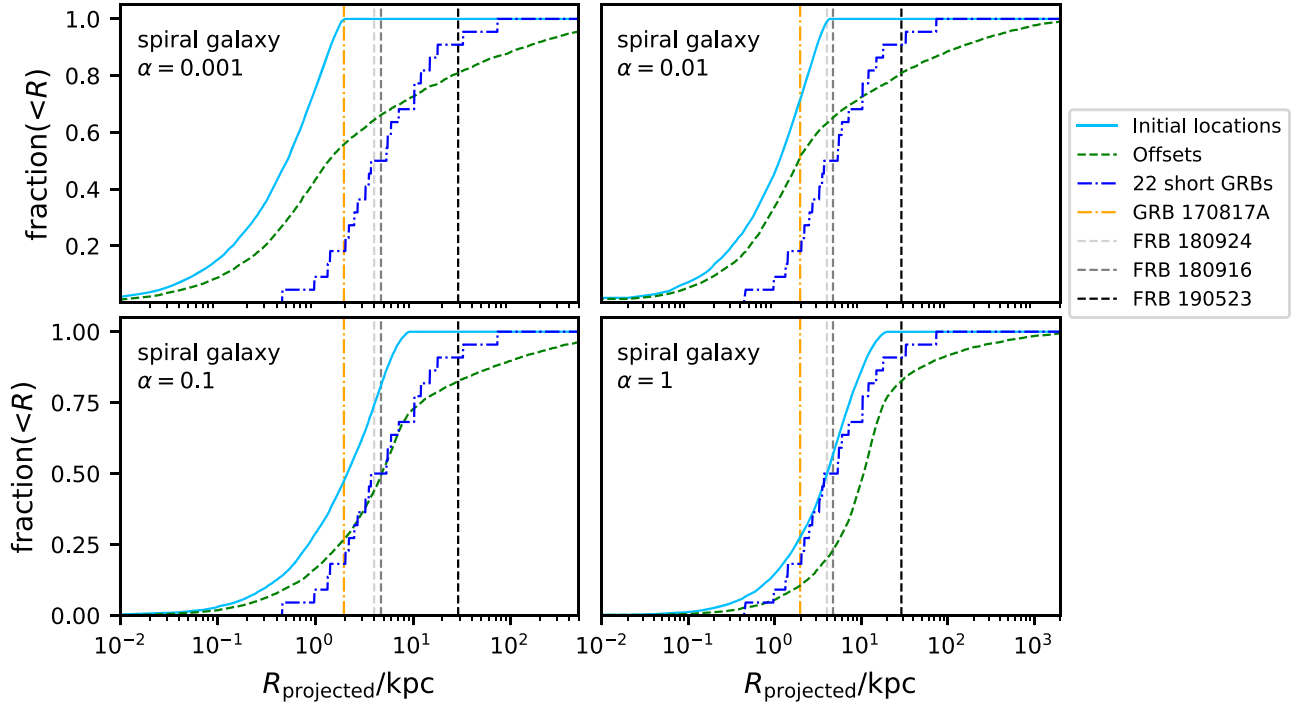


**Figure 4.** Initial location and offset cumulative distributions in spiral galaxies with different masses ( $\alpha = 0.001, 0.01, 0.1, 1$ ) for NS–NS mergers. The observed offsets of 22 short GRBs, GW170817/GRB 170817A, FRB 121102, FRB 180916, FRB 180924, and FRB 190523 are also shown.

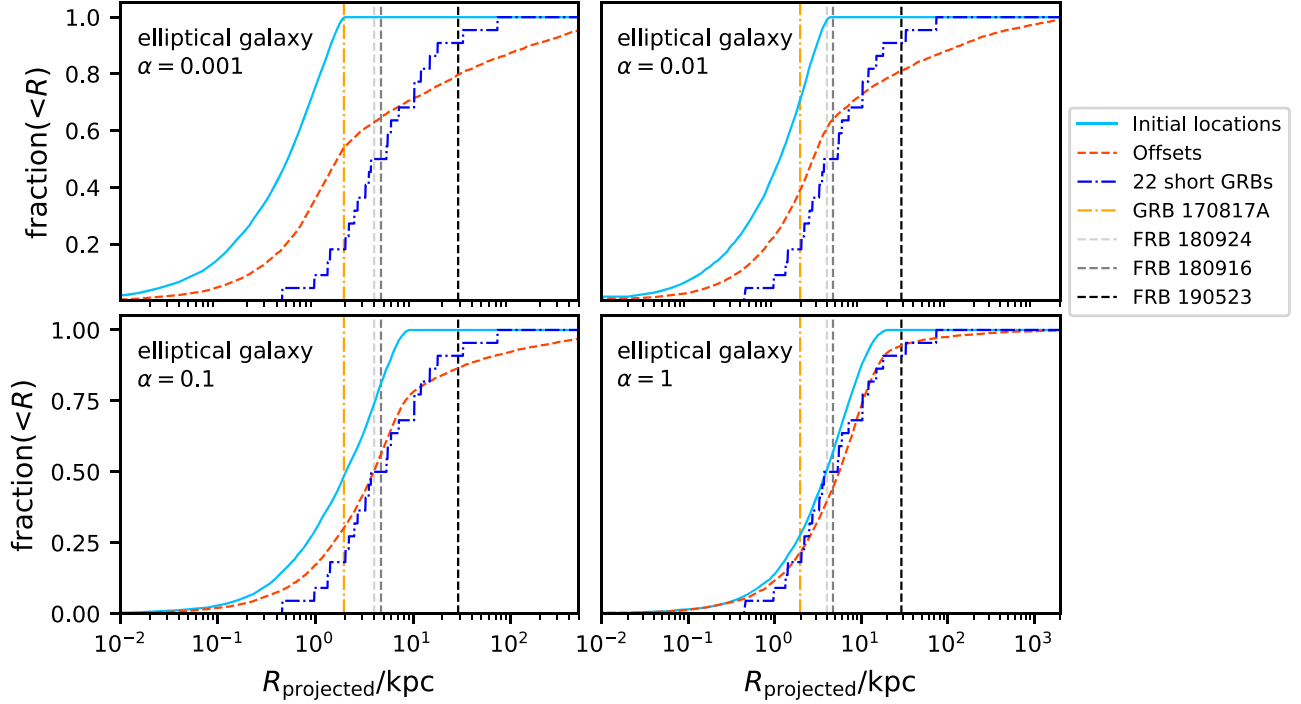


**Figure 5.** Initial location and offset cumulative distributions in elliptical galaxies with different masses ( $\alpha = 0.001, 0.01, 0.1, 1$ ) for NS–NS mergers. The observed offsets of 22 short GRBs, GW170817/GRB 170817A, FRB 121102, FRB 180916, FRB 180924, and FRB 190523 are also shown.

#### 4. Local Event Rate

Mergers of NS–NS and NS–black hole binaries have long been considered as the progenitors of short GRBs, which was confirmed by the discovery of GW170817/GRB 170817A (Abbott et al. 2017b). According to GW170817, the local rate of NS–NS mergers is  $\rho_0 = 1540_{-1220}^{+3200} \text{Gpc}^{-3} \text{yr}^{-1}$  (Abbott

et al. 2017). The local rate of short GRBs has been widely studied and found to range from several to several tens of  $\text{Gpc}^{-3} \text{yr}^{-1}$  (Guetta & Piran 2006; Nakar et al. 2006; Coward et al. 2012; Wanderman & Piran 2015; Tan et al. 2018; Zhang & Wang 2018). According to Zhang & Wang (2018), the local rate of short GRBs is  $7.53 \text{Gpc}^{-3} \text{yr}^{-1}$ . If the beaming

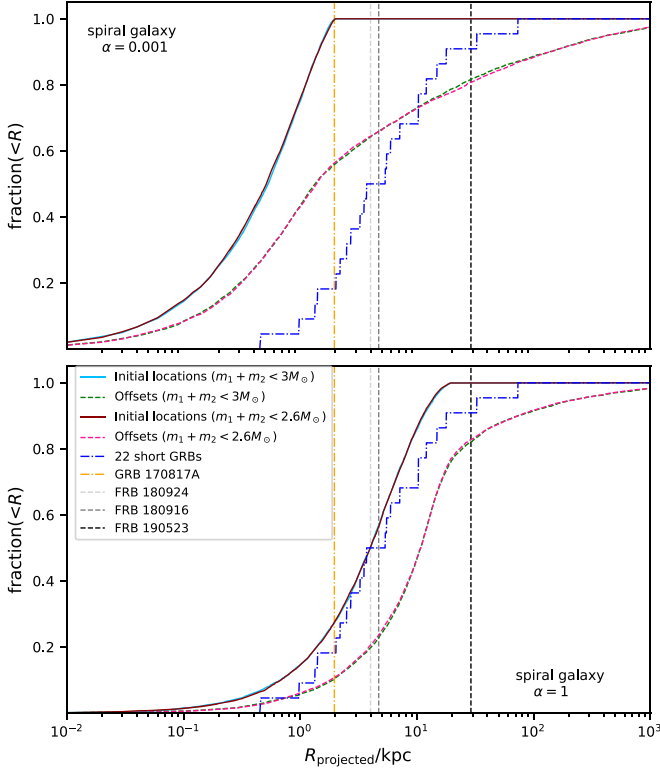


**Figure 6.** Initial location and offset cumulative distributions in spiral galaxies for NS–NS mergers that may produce NSs and observed offsets of short GRBs and FRBs.

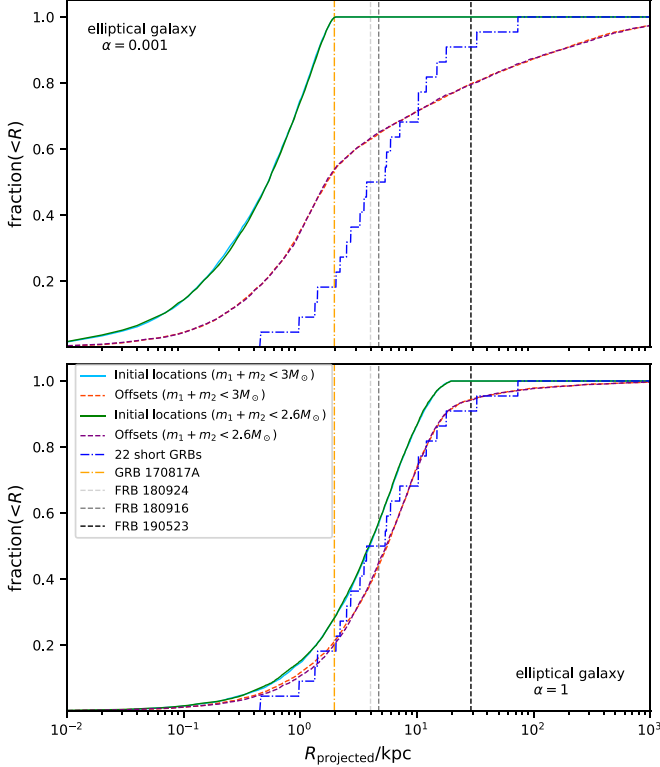


**Figure 7.** Initial location and offset cumulative distributions in elliptical galaxies for NS–NS mergers that may produce NSs and observed offsets of short GRBs and FRBs.

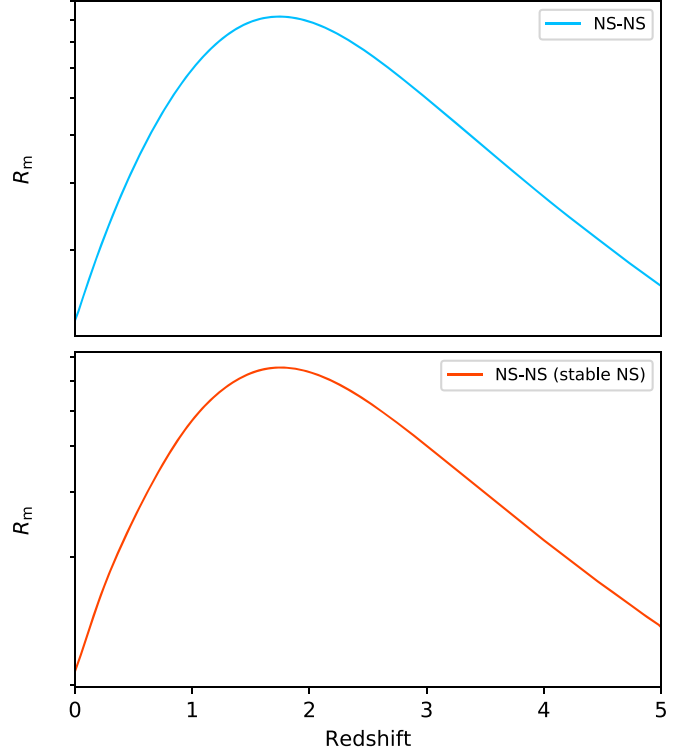


**Figure 8.** Merger rates  $R_m(z)$  as a function of redshift  $z$  for NS–NS mergers (upper panel), and NS–NS mergers that can produce NSs (bottom panel). Rates are in arbitrary units.

factor is chosen as  $27^{+158}_{-18}$  (Fong et al. 2015), the local event rate of all short GRBs is  $203^{+1152}_{-135} \text{Gpc}^{-3} \text{yr}^{-1}$ , which is broadly in agreement with the LIGO result (Abbott et al. 2017b).

As for the formation rate of non-repeating FRBs, we adopt the model and results given by Zhang & Wang (2019). In their calculation, considering the delay time, the cumulative redshift distribution can be derived as

$$N(<z) = T \frac{A}{4\pi} f \int_0^z \rho_{\text{FRB}}(z) \left[ \int_0^1 \eta(\varepsilon) \int_{E_{h/\varepsilon}}^{E_{\text{max}}} \Phi(E) dE d\varepsilon \right] \times \frac{dV(z)}{1+z}, \quad (18)$$

where  $T$  is the observation time,  $A$  is the sky area,  $\Phi(E)$  is the energy distribution,  $\eta(\varepsilon)$  is the beaming effect of the telescope, and  $\rho_{\text{FRB}}(z)$  is the formation rate of FRBs. We adopt the results of Parkes with time delay (Zhang & Wang 2019) and obtain the local formation rate as

$$\rho_0 \simeq 6 \times 10^4 \left( \frac{T}{270 \text{ s}} \right)^{-1} \left( \frac{A}{4\pi} \right)^{-1} f_b^{-1} \text{Gpc}^{-3} \text{yr}^{-1}, \quad (19)$$

where  $f_b$  is the beaming factor of the FRB, and the typical value of observation time is taken from Thornton et al. (2013). This local formation rate is consistent with the result of Cao et al. (2018). It is proposed that, during the final stages of a BNS merger inspiral, the interaction between the magnetosphere could also produce a non-repeating FRB (Totani 2013; Zhang 2014; Metzger & Zivancev 2016; Wang et al. 2016, 2018a). However, the rate of BNS mergers is well below the FRB rate, which is also discussed in Ravi (2019) for the CHIME sample.

On the other hand, many bursts can be produced by the remnant NSs from BNS mergers (Yamasaki et al. 2018). If the lifetime of each repeater is  $\tau$  yr, the volume density  $\rho_{\text{FRB}}\tau \sim 5 \times 10^3 \text{ Gpc}^{-3}$  is found by Wang & Zhang (2019) above the fluence limit  $F_{\text{min}} = 0.5 \text{ Jy ms}$ . The value of  $\tau$  is very uncertain, and relates to the activity of a newborn NS. The magnetic activity timescale in the direct Urca (high-mass NS) and modified Urca (normal-mass NS) case are about a few tens and a few hundred years, respectively (Beloborodov & Li 2016). For a lifetime of  $\tau \sim (10\text{--}100) \text{ yr}$ , the birth rate  $\rho_{\text{FRB}} \sim (50\text{--}500) \text{ Gpc}^{-3} \text{ yr}^{-1}$  can explain the observational properties of FRB 121102, such as energy distribution (Wang & Zhang 2019). In this case, the observed FRB rate is consistent with those of SLSNe and short GRBs (Wang & Zhang 2019).

## 5. Observational Properties of FRBs from BNS Mergers

Most FRB models invoke coherent radiation within the magnetosphere of a magnetized NS (e.g., Kumar et al. 2017; Yang & Zhang 2018; Wang & Lai 2019). Only the fluctuation of net charges with respect to the background outflow can make a contribution to coherent radiation (Yang & Zhang 2018). The fluctuation in the magnetosphere could be triggered by non-stationary sparks (Ruderman & Sutherland 1975), pulsar lightning (Katz 2017), starquake of the NS (Wang et al. 2018b), a nearby astrophysical plasma stream (Zhang 2017, 2018b), or exotic small bodies (Geng & Huang 2015; Dai et al. 2016). In this section, we calculate the coherent curvature radiation from the fluctuation of the magnetosphere, and predict observation properties from the ejecta of the BNS merger.

### 5.1. Coherent Curvature Radiation by Bunches

The extremely high brightness temperatures of FRBs require their radiation mechanisms to be coherent. Two coherent mechanisms are often considered in current FRB models: curvature radiation by bunches (Katz 2014, 2018a; Kumar et al. 2017; Ghisellini & Locatelli 2018; Yang & Zhang 2018) and maser mechanisms (Lyubarsky 2014; Beloborodov 2017; Ghisellini 2017; Waxman 2017; Lu & Kumar 2018; Metzger et al. 2019). Here, we mainly consider curvature radiation by bunches as the radiation mechanism of FRBs.

First, we briefly summarize curvature radiation by bunches following Yang & Zhang (2018). For a relativistic electron with Lorentz factor  $\gamma$  moving along a trajectory with curvature radius  $\rho$ , its radiation is beamed in a narrow cone of  $\sim 1/\gamma$  in the electron velocity direction. In the trajectory plane, the energy radiated per unit frequency interval per unit solid angle is (Jackson 1998)

$$\frac{dI}{d\omega d\Omega} \simeq \frac{e^2}{c} \left[ \frac{\Gamma(2/3)}{\pi} \right]^2 \left( \frac{3}{4} \right)^{1/3} \left( \frac{\omega\rho}{c} \right)^{2/3} e^{-\omega/\omega_c}, \quad (20)$$

where  $\omega_c = 3c\gamma^3/2\rho$  is the critical frequency of curvature radiation. We consider a three-dimensional bunch characterized by its length  $L$ , curvature radius  $\rho$ , and bunch opening angle<sup>6</sup>  $\varphi$ .

<sup>6</sup> Here the bunch opening angle is defined as the maximum angle between each electron trajectory (i.e., magnetic field line for curvature radiation) in a bunch; see Figures 9 and 10 in Yang & Zhang (2018). In the magnetosphere, given that the field lines are not parallel with each other, bunches will slightly expand when they move away from the dipole center.

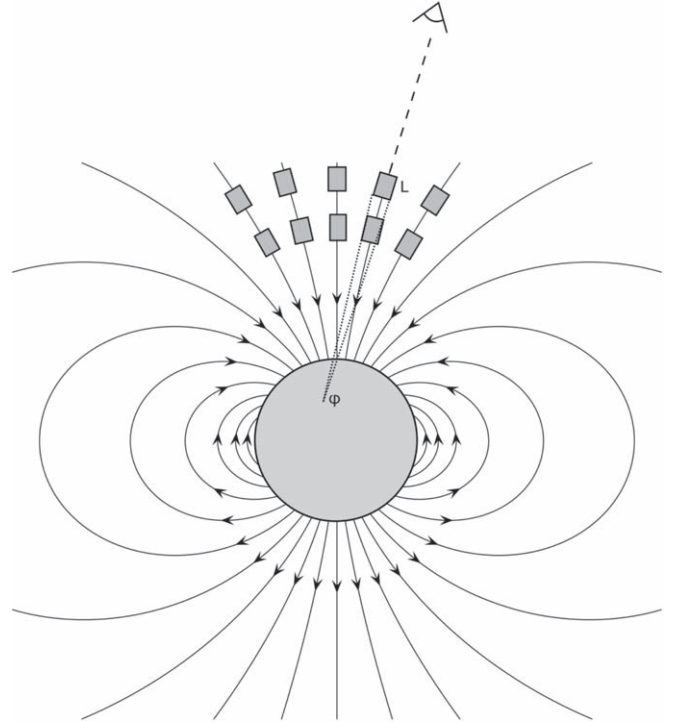


**Figure 9.** Cartoon for coherent curvature radiation by bunches in the magnetosphere. The gray dark regions denote bunches that are generated by the fluctuation of net charges with respect to the Goldreich–Julian background outflow.  $L$  is the bunch length, and  $\varphi$  is the bunch opening angle.

In the bunch, the electron energy distribution is assumed to be

$$N_e(\gamma)d\gamma = N_{e,0}(\gamma/\gamma_m)^{-p}d\gamma \quad \text{for} \quad \gamma_m < \gamma < \gamma_M. \quad (21)$$

$N_e$  is defined as the net charge number of electrons in a bunch, given that only the net charged particles contribute to the coherent curvature radiation. Then the curvature radiation spectra are characterized by a multi-segment broken power law (see Figures 11 and 12 in Yang & Zhang 2018), with the break frequencies defined by

$$\nu_l = \frac{c}{\pi L}, \quad \nu_\varphi = \frac{3c}{2\pi\rho\varphi^3} \quad \text{and} \quad \nu_c = \frac{3c\gamma_m^3}{4\pi\rho}. \quad (22)$$

The emitted energy at the peak frequency  $\nu_{\text{peak}}$  is given by (Yang & Zhang 2018)

$$\left. \frac{dI}{d\omega d\Omega} \right|_{\text{peak}} \simeq \frac{e^2}{c} K(p) N_{e,0}^2 \gamma_m^4 \left( \frac{\nu_{\text{peak}}}{\nu_c} \right)^{2/3}, \quad (23)$$

where  $K(p) = 2^{(2p-6)/3} [\Gamma(2/3)\Gamma(p-1/3)]^2 / 3\pi^2$ , and the peak frequency is given by  $\nu_{\text{peak}} = \min(\nu_l, \nu_\varphi, \nu_c)$ .

For a single source, e.g., a charged particle or bunch, the frequency-dependent duration of the curvature radiation is  $T \sim (1 - v/c)\rho/\gamma c \sim \rho/2c\gamma^3 \sim 1/\nu_c$ . If the electromagnetic wave frequency is considered to be  $\nu_c \sim 10^9 \text{ Hz}$ , which corresponds to the typical FRB frequency, the pulse duration of the curvature radiation will be  $T \sim 1/\nu_c \sim 1 \text{ ns}$ , which is much less than the observed FRB duration,  $T_{\text{obs}} \sim 1 \text{ ms}$ . Therefore, there must be numerous bunches sweeping across the line of sight during the observed duration  $T_{\text{obs}}$  (Yang & Zhang 2018), as shown in Figure 9. Assuming that the radiation from numerous bunches is incoherent at the observed frequency  $\nu \sim 1 \text{ GHz}$ , the observed flux density satisfies

(Yang & Zhang 2018)

$$F_\nu = \frac{2\pi}{TD^2} \frac{dI}{d\omega d\Omega}, \quad (24)$$

where  $D$  is the source distance and  $T$  is the mean time interval between adjacent bunches. If the bunches are generated via plasma instability, the gap between adjacent bunches may be of the order of the bunch scale itself, which gives  $T \sim L/c$ . Thus, the observed peaked flux density is

$$F_{\nu,\text{peak}} \simeq \frac{2\pi e^2}{c} K(p) \frac{N_{e,0}^2 \gamma_m^4}{D^2 T} \left( \frac{\nu_{\text{peak}}}{\nu_c} \right)^{2/3}. \quad (25)$$

Due to  $\nu_{\text{peak}} \leq \nu_c$ , the observed peak flux density must be less than the limit flux density

$$F_{\nu,\text{limit}} = \frac{2\pi e^2}{c} K(p) \frac{N_{e,0}^2 \gamma_m^4}{D^2 T}. \quad (26)$$

### 5.2. FRBs from the Pulsar Magnetosphere

As pointed out by Yang & Zhang (2018), only the fluctuation of net charges with respect to the background outflow can make a contribution to coherent radiation. We define the fraction between the fluctuating net charge density  $\delta n_{\text{GJ}}$  and the background Goldreich–Julian density  $n_{\text{GJ}}$  as

$$\mu_c = \frac{\delta n_{\text{GJ}}}{n_{\text{GJ}}}, \quad (27)$$

where one has  $N_{e,\text{tot}} = \gamma_m N_{e,0}/(p-1) = \mu_c n_{\text{GJ}} V$ , where  $V$  is the bunch volume. When the bunches move along the field lines in the pulsar magnetosphere, the bunch opening angle  $\varphi$  will depend on the magnetic field configure, as shown in Figure 9. If the emission region is close to the magnetic axis, we consider that  $\varphi \sim \theta$ , where  $\theta$  is the polar angle. Therefore, the transverse size of a bunch is  $\sim r\varphi \sim \rho\varphi^2$ , where  $r \sim \rho\theta$  is the bunch distance related to the center of the magnetic dipole<sup>7</sup>. The bunch volume is  $V \sim L(\rho\varphi^2)^2 \simeq L\rho^2\varphi^4$ , and one has

$$N_{e,0} = (p-1)\gamma_m^{-1}\mu_c n_{\text{GJ}} L\rho^2\varphi^4 \quad (28)$$

On the other hand, the background Goldreich–Julian density is

$$n_{\text{GJ}} = \frac{B}{Pec} \left( \frac{r}{R} \right)^{-3} \sim \frac{BR^3}{ecP\rho^3\varphi^3}, \quad (29)$$

where  $B$  is the pulsar surface magnetic field strength,  $P$  is the pulsar period, and  $R$  is the pulsar radius. According to Equations (26), (28), (29), and  $T \sim L/c$ , one finally has

$$\begin{aligned} F_{\nu,\text{limit}} &\simeq \frac{2\pi(p-1)^2 K(p)}{c^2} \frac{\mu_c^2 \gamma_m^2 L B^2 R^6 \varphi^2}{D^2 P^2 \rho^2} \\ &\simeq 3 \text{ Jy} \mu_c^2 \gamma_{m,2}^2 L_1 B_{14}^2 R_6^6 \varphi_{-2}^2 D_{\text{Gpc}}^{-2} P_{-1}^{-2} \rho_7^{-2}, \end{aligned} \quad (30)$$

where the convention  $Q_x = Q/10^x$  in cgs units is adopted,  $D_{\text{Gpc}} = D/1 \text{ Gpc}$ , and  $(p-1)^2 K(p) = 0.4542$  for  $p = 3$ . The intrinsic spectrum is a multi-segment broken power

law<sup>8</sup> with break frequencies of  $\nu_l$ ,  $\nu_\varphi$ , and  $\nu_c$  (Yang & Zhang 2018). In the above equation, we take  $L \sim 10 \text{ cm}$ ,  $\varphi \sim 0.01$ ,  $\gamma_m \sim 100$ , and  $\rho \sim 10^7 \text{ cm}$ , which give  $\nu_l \sim \nu_\varphi \sim \nu_c \simeq 1 \text{ GHz}$  according to Equation (22). In this case, the spectrum above a few GHz would be very soft (with spectral index of  $-(2p+4)/3$  as discussed in Yang & Zhang 2018), which might explain the high-frequency cutoff of FRB observation. Meanwhile, if we consider that the observed narrow spectrum is due to a very soft spectrum at high frequency and radio absorption at low frequency (free-free absorption, synchrotron self-absorption, plasma absorption, etc.) the condition of the above typical frequencies at a few GHz would cause the limit flux to be a minimum, which would give a strongest constraint on these parameters. For an FRB with observed flux density of  $F_\nu \sim$  a few Jy, its progenitor could be a young magnetar with  $B \gtrsim 10^{14} \text{ G}$  and  $P \lesssim 0.1 \text{ s}$ , which could cause a large observed flux density limit  $F_\nu$ , limit.

After the BNS merger, the newborn NS with a surface dipole magnetic field strength  $B$  and initial period  $P_0$  would spin down due to magnetic torques, the spin-down luminosity  $L_{\text{sd}}$  being given by (e.g., Yang et al. 2019)

$$\begin{aligned} L_{\text{sd}} &= L_{\text{sd},0} \left( 1 + \frac{t}{t_{\text{sd}}} \right)^{-2} \\ &\simeq 10^{43} \text{ erg s}^{-1} \begin{cases} 0.4 B_{14}^{-2} t_{\text{yr}}^{-2} & \text{for late time } t \gg t_{\text{sd}} \\ B_{12}^2 P_{0,-3}^{-4} & \text{for early time } t \ll t_{\text{sd}} \end{cases} \end{aligned} \quad (31)$$

where  $L_{\text{sd},0} = I\Omega_0^2/2t_{\text{sd}} \simeq 10^{47} \text{ erg s}^{-1} B_{14}^2 P_{0,-3}^{-4}$  is the initial spin-down power,  $t_{\text{sd}} = 3c^3 I/B^2 R^6 \Omega_0^2 = 2 \times 10^5 \text{ s} B_{14}^{-2} P_{0,-3}^2$  is the spin-down timescale,  $I = 10^{45} \text{ g cm}^2$  is the moment of inertia of the neutron star, and  $\Omega_0 = 2\pi/P_0$  is the initial angular velocity of the NS. According to the above equation, in order to have the spin-down luminosity at the same order of magnitude as the isotropic luminosity of FRBs when an FRB occurs, for the late-time case, the NS is required to be a magnetar with magnetic field  $B \sim 10^{14} \text{ G}$ , and for the early-time case, it is required to be a normal pulsar with magnetic field  $B \sim 10^2 \text{ G}$ . Due to the rotation energy loss, the spin period will increase with time, e.g.,

$$\begin{aligned} P &= P_0 \left( 1 + \frac{t}{t_{\text{sd},0}} \right)^{1/2} \\ &\simeq 1 \text{ ms} \begin{cases} 12 B_{14} t_{\text{yr}}^{1/2} & \text{for late time } t \gg t_{\text{sd}} \\ P_{0,-3} & \text{for early time } t \ll t_{\text{sd}} \end{cases}. \end{aligned} \quad (32)$$

Therefore, for a magnetar with  $B \sim 10^{14} \text{ G}$  and  $P_0 \sim 1 \text{ ms}$ , when its period increases to  $P \lesssim 0.1 \text{ s}$ , the magnetar age is required to be  $t \lesssim 100 \text{ yr}$ . On the other hand, if the radio bursts are powered by the rotational energy, e.g.,  $L_{\text{sd}} \gtrsim f_b L_{\text{FRB}}$ , where  $L_{\text{FRB}} \sim 10^{42} \text{ erg s}^{-1}$  is the FRB isotropic luminosity,

<sup>7</sup> According to the geometry of the magnetic dipole field (e.g., see Appendix G of Yang & Zhang 2018), the curvature radius at  $(r, \theta)$  is  $\rho \simeq 4r/3 \sin \theta$  for  $\theta \lesssim 0.5$ .

<sup>8</sup> In general, for a bunch with uniform distributed charge density, its curvature radiation appears as a wide spectrum, i.e.,  $\Delta\nu \sim \nu$  (Yang & Zhang 2018). The observed structure might be due to scintillation, plasma lensing (Cordes et al. 2017), or spatial structure of a clumpy radiating charge distribution (Katz 2018a).

and  $f_b$  is the beaming factor, the magnetar is required to be very young with

$$t < 2 \text{ yr } f_b^{-1/2} L_{\text{FRB},42}^{-1/2} B_{14}^{-1}. \quad (33)$$

The rotational energy seems not to be viable as the FRB power source for a magnetar, for the following reasons: (1) the spindown timescale of the rapidly spinning magnetar would be shorter than the observation time of FRB 121102 (Katz 2016a, 2018b), which is of the order of several years; (2) a young ejecta associated with a magnetar with age of  $t \ll 1$  yr would involve an observable DM decreasing (e.g., Piro 2016; Yang & Zhang 2017, see the next section), which is contrary to the observation of FRB 121102 (Hessels et al. 2019; Josephy et al. 2019); (3) the distribution of DMs of non-repeating FRBs is inconsistent with that of expanding supernova remnants (Katz 2016b). Therefore, other power sources would be necessary, e.g., magnetic power (Metzger et al. 2017), gravitational power (Geng & Huang 2015; Dai et al. 2016), and kinetic power (Zhang 2017, 2018b).

### 5.3. Observation Properties from the Ejecta of BNS Mergers

In this section, we consider the observation properties of the ejecta of BNS mergers. Compared with a supernova from core-collapse explosion, the ejecta from a BNS merger has higher velocity  $v \sim (0.1 - 0.3)c$  and lower mass  $M \sim (10^{-4} - 10^{-2})M_\odot$ . At time  $t$  after the BNS merger, the ejecta electron density is

$$n_e \simeq \frac{\eta Y_e M}{4\pi m_p v^3 t^3} = 2.8 \text{ cm}^{-3} \eta Y_{e,0.2} M_{-3} v_{0.2}^{-3} t_{\text{yr}}^{-3}, \quad (34)$$

where  $n_e$  is the free electron density,  $\Delta R \sim vt$  is the ejecta thickness,  $Y_e = 0.2 Y_{e,0.2}$  is the electron fraction,  $\eta$  is the ionization fraction,  $M_{-3} = M/10^{-3}M_\odot$ , and  $v_{0.2} = v/0.2c$ . Due to  $\nu_{\text{FRB}} \sim 1 \text{ GHz} \gg \nu_p \simeq 10^4 \text{ Hz} \sqrt{n_e} \sim 17 \text{ kHz}$ , the ejecta plasma is transparent for a FRB. Besides, for an extremely young ejecta, the FRB emission may be subject to a large free-free opacity, so that the FRB may not be detected. The free-free optical depth is

$$\begin{aligned} \tau_{\text{ff}} &= \alpha_{\text{ff}} \Delta R \simeq (0.018 T_{\text{eje}}^{-3/2} Z^2 n_e n_i \nu^{-2} \bar{g}_{\text{ff}}) \Delta R \\ &= 2.7 \times 10^{-8} \eta^2 Y_{e,0.2}^2 M_{-3}^2 T_{\text{eje},4}^{-3/2} \nu_9^{-2} v_{0.2}^{-5} t_{\text{yr}}^{-5}, \end{aligned} \quad (35)$$

where  $T_{\text{eje}} = 10^4 T_{\text{eje},4} \text{ K}$  is the ejecta temperature,  $\bar{g}_{\text{ff}} \sim 1$  is the Gaunt factor,  $n_i$  and  $n_e$  are the number densities of ions and electrons, respectively, and  $n_i \sim n_e$  and  $Z \sim 1$  are assumed in the ejecta. Thus, the ejecta will transparent for the free-free absorption a few weeks after the BNS merger.

Next, we discuss the DM and rotation measure (RM) from the ejecta. The DM contributed by the ejecta is

$$\begin{aligned} \text{DM} &= n_e \Delta R \simeq \frac{\eta Y_e M}{4\pi m_p v^2 t^2} \simeq 0.17 \text{ pc cm}^{-3} \\ &\eta Y_{e,0.2} M_{-3} v_{0.2}^{-2} t_{\text{yr}}^{-2}. \end{aligned} \quad (36)$$

We can see that the DM contributed by the ejecta is small. Only when  $t \lesssim 1$  yr can the ejecta contribute an observable DM variation. On the other hand, when the ejecta expands outward, the magnetic flux within it is unchanged. The total magnetic flux in the ejecta may be  $\Phi \sim BR^2 \simeq 10^{26} \text{ G cm}^2 B_{14} R_6^2$ . Due to the conservation of magnetic flux, one has  $\Phi \sim B_{\text{eje}}(vt)^2 \sim BR^2$ ,

where  $B_{\text{eje}}$  is the magnetic field strength in the ejecta. Finally, the RM contributed by the ejecta at time  $t$  is

$$\begin{aligned} |\text{RM}| &= \frac{e^3 B_{\text{eje}}}{2\pi m_e^2 c^4} n_e \Delta R \sim \frac{e^3}{2\pi m_e^2 c^4} \xi BR^2 v^{-2} t^{-2} \text{DM} \\ &\sim 4 \times 10^{-4} \text{ rad m}^{-2} \xi \eta Y_{e,0.2} B_{14} R_6^2 M_{-3} v_{0.2}^{-4} t_{\text{yr}}^{-4}, \end{aligned} \quad (37)$$

where the magnetic configure factor  $\xi$  is defined as  $\xi \equiv \langle B_{\parallel} \rangle / \langle B \rangle$ . Notice that the RM would decrease faster than the DM, since the magnetic field in the ejecta also decreases with time, e.g.,  $B_{\text{eje}} \propto t^{-2}$ . In summary, for ejecta with age of  $t \gtrsim 1$  yr, the corresponding DM and RM are very small.

## 6. Conclusions and Discussion

Motivated by the large offsets of FRB 180924, FRB 180916, and FRB 190523, we study FRBs from activities of NSs newborn in BNS mergers. FRB 180924 and FRB 190523 are localized to massive galaxies with low SFR, which are dramatically different to the host galaxy of FRB 121102. First, we use the latest binary-evolution code BSE to calculate the properties of NS–NS binaries. The merger time from population synthesis shows a similar distribution to the gravitational wave delay time distribution, i.e.,  $dN/dt \propto t^{-1}$  at late times. We show that the host galaxies and offsets of FRB 180924, FRB 180916, and FRB 190523 are well-matched to the distributions for NS–NS mergers from population synthesis. In addition, using the galaxy model with similar mass to a short GRB host galaxy, the offset distribution of short GRBs is well reproduced from population synthesis.

The observational properties of FRBs from the BNS merger channel are also discussed. In this work, we consider that FRBs are formed by coherent curvature radiation in the magnetosphere of NSs (Yang & Zhang 2018). Due to some accidental events, e.g., NS starquake (Wang et al. 2018b), nearby astrophysical plasma (Zhang 2017, 2018b), or exotic small bodies (Geng & Huang 2015; Dai et al. 2016), the magnetosphere is disturbed, and the fluctuation of net charges with respect to the background Goldreich–Julian outflow would cause coherent curvature radiation. The observed flux of FRBs requires that the NS has a large magnetic field,  $B \gtrsim 10^{14} \text{ G}$ , and fast rotation,  $P \lesssim 0.1 \text{ s}$ , which correspond to a young magnetar with an age of  $t \lesssim 100 \text{ yr}$  and initial period of  $P_0 \sim 1 \text{ ms}$ . Since the ejecta of the BNS merger has high velocity,  $v \sim (0.1 - 0.3)c$ , and low mass,  $M \sim (10^{-4} - 10^{-2})M_\odot$ , the ejecta will be transparent for free-free absorption a few weeks after the BNS merger, and the corresponding DM and RM are very small for ejecta with an age of  $t \gtrsim 1 \text{ yr}$ .

In the BNS merger scenario, it is possible that we observe associations of FRBs with short GRBs and GW events. In the future, if more FRBs are localized, the offset distribution of short GRBs can be compared with that of FRBs. Since a magnetar born in a BNS merger can show magnetic activity for a long time (Beloborodov & Li 2016; Beloborodov 2019), we can search for FRBs in the location region of short GRBs and BNS merger GW events.

We thank the anonymous referee for detailed and very constructive suggestions that have allowed us to improve our manuscript. We thank Sambaran Banerjee for sharing the updated BSE code. We also thank Yong Shao and Xiangdong Li for helpful discussions. This work is supported by the

National Natural Science Foundation of China (grants U1831207, 1573014, 11833003, 1185130, 11573021, and U1938104) and the National Key Research and Development Program of China (grant 2017YFA0402600).

### ORCID iDs

F. Y. Wang  <https://orcid.org/0000-0003-4157-7714>  
 Yuan-Pei Yang  <https://orcid.org/0000-0001-6374-8313>  
 Z. G. Dai  <https://orcid.org/0000-0002-7835-8585>

### References

- Aarseth, S. J. 2012, *MNRAS*, **422**, 841  
 Abbott, B. P., Abbott, R., Abbott, T. D., et al. 2017a, *PhRvL*, **119**, 161101  
 Abbott, B. P., Abbott, R., Abbott, T. D., et al. 2017b, *ApJL*, **848**, L13  
 Ai, S., Gao, H., & Zhang, B. 2019, arXiv:1912.06369  
 Bajkova, A., & Bobylev, V. 2017, *OAst*, **26**, 72  
 Banerjee, S., Belczynski, K., Fryer, C. L., et al. 2019, arXiv:1902.07718  
 Bannister, K. W., Deller, A. T., Phillips, C., et al. 2019, *Sci*, **365**, 565  
 Barthelmy, S. D., Chincarini, G., Burrows, D. N., et al. 2005, *Natur*, **438**, 994  
 Belczynski, K., Bulik, T., Fryer, C. L., et al. 2010, *ApJ*, **714**, 1217  
 Belczynski, K., Bulik, T., & Rudak, B. 2002, *ApJ*, **571**, 394  
 Belczynski, K., Heger, A., Gladysz, W., et al. 2016, *A&A*, **594**, A97  
 Belczynski, K., Kalogera, V., Rasio, F. A., et al. 2008, *ApJS*, **174**, 223  
 Belczynski, K., Perna, R., Bulik, T., et al. 2006, *ApJ*, **648**, 1110  
 Beloborodov, A. M. 2017, *ApJL*, **843**, L26  
 Beloborodov, A. M. 2019, arXiv:1908.07743  
 Beloborodov, A. M., & Li, X. 2016, *ApJ*, **833**, 261  
 Beniamini, P., & Piran, T. 2019, *MNRAS*, **487**, 4847  
 Berger, E. 2014, *ARA&A*, **52**, 43  
 Bethe, H. A., & Brown, G. E. 1998, *ApJ*, **506**, 780  
 Bloom, J. S., Prochaska, J. X., Pooley, D., et al. 2006, *ApJ*, **638**, 354  
 Bloom, J. S., Sigurdsson, S., & Pols, O. R. 1999, *MNRAS*, **305**, 763  
 Cao, X.-F., Yu, Y.-W., & Zhou, X. 2018, *ApJ*, **858**, 89  
 Champion, D. J., Petroff, E., Kramer, M., et al. 2016, *MNRAS*, **460**, L30  
 Chatterjee, S., Law, C. J., Wharton, R. S., et al. 2017, *Natur*, **541**, 58  
 Cheng, Y., Zhang, G. Q., & Wang, F. Y. 2020, *MNRAS*, **491**, 1498  
 Cordes, J. M., & Chatterjee, S. 2019, *ARA&A*, **57**, 417  
 Cordes, J. M., Wasserman, I., Hessels, J. W. T., et al. 2017, *ApJ*, **842**, 35  
 Coward, D. M., Howell, E. J., Piran, T., et al. 2012, *MNRAS*, **425**, 2668  
 Dai, Z. G., Wang, J. S., Wu, X. F., & Huang, Y. F. 2016, *ApJ*, **829**, 27  
 Dai, Z. G., Wang, X. Y., Wu, X. F., & Zhang, B. 2006, *Sci*, **311**, 1127  
 de Mink, S. E., & Belczynski, K. 2015, *ApJ*, **814**, 58  
 Duquenois, A., & Mayor, M. 1991, *A&A*, **500**, 337  
 Fong, W., Berger, E., Chornock, R., et al. 2013, *ApJ*, **769**, 56  
 Fong, W., Berger, E., & Fox, D. B. 2010, *ApJ*, **708**, 9  
 Fong, W., Berger, E., Margutti, R., & Zauderer, B. A. 2015, *ApJ*, **815**, 102  
 Fox, D. B., Frail, D. A., Price, P. A., et al. 2005, *Natur*, **437**, 845  
 Fryer, C. L., Belczynski, K., Wiktorowicz, G., et al. 2012, *ApJ*, **749**, 91  
 Fryer, C. L., Woosley, S. E., & Hartmann, D. H. 1999, *ApJ*, **526**, 152  
 Gao, H., Li, Z., & Zhang, B. 2014, *ApJ*, **788**, 189  
 Gao, H., Zhang, B., & Lü, H.-J. 2016, *PhRvD*, **93**, 044065  
 Gehrels, N., Sarazin, C. L., O'Brien, P. T., et al. 2005, *Natur*, **437**, 851  
 Geng, J. J., & Huang, Y. F. 2015, *ApJ*, **809**, 24  
 Ghisellini, G. 2017, *MNRAS*, **465**, L30  
 Ghisellini, G., & Locatelli, N. 2018, *A&A*, **613**, A61  
 Guetta, D., & Piran, T. 2006, *A&A*, **453**, 823  
 Hansen, B. M. S., & Phinney, E. S. 1997, *MNRAS*, **291**, 569  
 Hernquist, L. 1990, *ApJ*, **356**, 359  
 Hessels, J. W. T., Spitler, L. G., Seymour, A. D., et al. 2019, *ApJL*, **876**, L23  
 Hurley, J. R., Tout, C. A., & Pols, O. R. 2002, *MNRAS*, **329**, 897  
 Jackson, J. D. 1998, *Classical Electrodynamics* (3rd; New York: Wiley)  
 Josephy, A., Chawla, P., Fonseca, E., et al. 2019, *ApJL*, **882**, L18  
 Katz, J. I. 1975, *Natur*, **253**, 698  
 Katz, J. I. 2014, *PhRvD*, **89**, 103009  
 Katz, J. I. 2016a, *MPLA*, **31**, 1630013  
 Katz, J. I. 2016b, *ApJ*, **826**, 226  
 Katz, J. I. 2017, *MNRAS*, **469**, L39  
 Katz, J. I. 2018a, *MNRAS*, **481**, 2946  
 Katz, J. I. 2018b, *PrPNP*, **103**, 1  
 Kulkarni, S. R., Ofek, E. O., Neill, J. D., Zheng, Z., & Juric, M. 2014, *ApJ*, **797**, 70  
 Kumar, P., Lu, W., & Bhattacharya, M. 2017, *MNRAS*, **468**, 2726  
 Levan, A. J., Lyman, J. D., Tanvir, N. R., et al. 2017, *ApJL*, **848**, L28  
 Li, Y., Zhang, B., Nagamine, K., & Shi, J. 2019a, *ApJL*, **884**, L26  
 Li, Z., Gao, H., Wei, J.-J., et al. 2019b, *ApJ*, **876**, 146  
 Li, Z.-X., Gao, H., Ding, X.-H., Wang, G.-J., & Zhang, B. 2018, *NatCo*, **9**, 3833  
 Liu, B., Li, Z., Gao, H., & Zhu, Z.-H. 2019, *PhRvD*, **99**, 123517  
 Lorimer, D. R., Bailes, M., McLaughlin, M. A., Narkevic, D. J., & Crawford, F. 2007, *Sci*, **318**, 777  
 Lü, H.-J., Zhang, B., Lei, W.-H., Li, Y., & Lasky, P. D. 2015, *ApJ*, **805**, 89  
 Lu, W., & Kumar, P. 2016, *MNRAS*, **461**, L122  
 Lu, W., & Kumar, P. 2018, *MNRAS*, **477**, 2470  
 Lyubarsky, Y. 2014, *MNRAS*, **442**, L9  
 Madau, P., & Dickinson, M. 2014, *ARA&A*, **52**, 415  
 Marcote, B., Nimmo, K., Hessels, J. W. T., et al. 2020, *Natur*, **577**, 190  
 Marcote, B., Paragi, Z., Hessels, J. W. T., et al. 2017, *ApJL*, **834**, L8  
 Margalit, B., Berger, E., & Metzger, B. D. 2019, *ApJ*, **886**, 110  
 Metzger, B. D., Berger, E., & Margalit, B. 2017, *ApJ*, **841**, 14  
 Metzger, B. D., Margalit, B., & Sironi, L. 2019, *MNRAS*, **485**, 4091  
 Metzger, B. D., Quataert, E., & Thompson, T. A. 2008, *MNRAS*, **385**, 1455  
 Metzger, B. D., & Zivancev, C. 2016, *MNRAS*, **461**, 4435  
 Miyamoto, M., & Nagai, R. 1975, *PASJ*, **27**, 533  
 Murase, K., Kashiyama, K., & Mészáros, P. 2016, *MNRAS*, **461**, 1498  
 Nakar, E., Gal-Yam, A., & Fox, D. B. 2006, *ApJ*, **650**, 281  
 Navarro, J. F., Frenk, C. S., & White, S. D. M. 1996, *ApJ*, **462**, 563  
 Nicholl, M., Williams, P. K. G., Berger, E., et al. 2017, *ApJ*, **843**, 84  
 Paczynski, B. 1990, *ApJ*, **348**, 485  
 Perna, R., & Belczynski, K. 2002, *ApJ*, **570**, 252  
 Petroff, E., Hessels, J. W. T., & Lorimer, D. R. 2019, *A&ARv*, **27**, 4  
 Piran, T. 1992, *ApJL*, **389**, L45  
 Piro, A. L. 2016, *ApJL*, **824**, L32  
 Platts, E., Weltman, A., Walters, A., et al. 2019, *PhR*, **821**, 1  
 Podsiadlowski, P., Langer, N., Poelarends, A. J. T., et al. 2004, *ApJ*, **612**, 1044  
 Popov, S. B., & Postnov, K. A. 2013, arXiv:1307.4924  
 Ravi, V. 2019, *NatAs*, **3**, 928  
 Ravi, V., Catha, M., D'Addario, L., et al. 2019, arXiv:1907.01542  
 Rowlinson, A., O'Brien, P. T., Metzger, B. D., Tanvir, N. R., & Levan, A. J. 2013, *MNRAS*, **430**, 1061  
 Ruderman, M. A., & Sutherland, P. G. 1975, *ApJ*, **196**, 51  
 Sana, H., de Mink, S. E., de Koter, A., et al. 2012, *Sci*, **337**, 444  
 Scalo, J. M. 1986, *FCPh*, **11**, 1  
 Shannon, R. M., Macquart, J. P., Bannister, K. W., et al. 2018, *Natur*, **562**, 386  
 Tan, W.-W., Fan, X.-L., & Wang, F. Y. 2018, *MNRAS*, **475**, 1331  
 Tendulkar, S. P., Bassa, C. G., Cordes, J. M., et al. 2017, *ApJL*, **834**, L7  
 Thornton, D., Stappers, B., Bailes, M., et al. 2013, *Sci*, **341**, 53  
 Totani, T. 2013, *PASJ*, **65**, L12  
 Totani, T., Morokuma, T., Oda, T., Doi, M., & Yasuda, N. 2008, *PASJ*, **60**, 1327  
 Voss, R., & Tauris, T. M. 2003, *MNRAS*, **342**, 1169  
 Walters, A., Weltman, A., Gaensler, B. M., Ma, Y.-Z., & Witzemann, A. 2018, *ApJ*, **856**, 65  
 Wanderman, D., & Piran, T. 2015, *MNRAS*, **448**, 3026  
 Wang, F. Y., & Dai, Z. G. 2013, *NatPh*, **9**, 465  
 Wang, F. Y., & Yu, H. 2017, *JCAP*, **03**, 023  
 Wang, F. Y., & Zhang, G. Q. 2019, *ApJ*, **882**, 108  
 Wang, J.-S., & Lai, D. 2019, arXiv:1907.12473  
 Wang, J.-S., Peng, F.-K., Wu, K., & Dai, Z.-G. 2018a, *ApJ*, **868**, 19  
 Wang, J.-S., Yang, Y.-P., Wu, X.-F., Dai, Z.-G., & Wang, F.-Y. 2016, *ApJL*, **822**, L7  
 Wang, W., Luo, R., Yue, H., et al. 2018b, *ApJ*, **852**, 140  
 Wang, Y. K., & Wang, F. Y. 2018, *A&A*, **614**, A50  
 Waxman, E. 2017, *ApJ*, **842**, 34  
 Wei, J.-J., Gao, H., Wu, X.-F., & Mészáros, P. 2015, *PhRvL*, **115**, 261101  
 Yamasaki, S., Totani, T., & Kiuchi, K. 2018, *PASJ*, **70**, 39  
 Yang, Y.-P., & Zhang, B. 2016, *ApJL*, **830**, L31  
 Yang, Y.-P., & Zhang, B. 2017, *ApJ*, **847**, 22  
 Yang, Y.-P., & Zhang, B. 2018, *ApJ*, **868**, 31  
 Yang, Y.-P., Zhang, B., & Wei, J.-Y. 2019, *ApJ*, **878**, 89  
 Yu, H., & Wang, F. Y. 2017, *A&A*, **606**, A3  
 Yu, H., & Wang, F. Y. 2018, *EPJIC*, **78**, 692  
 Zhang, B. 2014, *ApJL*, **780**, L21  
 Zhang, B. 2017, *ApJL*, **836**, L32  
 Zhang, B. 2018a, *ApJL*, **867**, L21  
 Zhang, B. 2018b, *ApJL*, **854**, L21  
 Zhang, B. 2020, arXiv:2002.00335  
 Zhang, G. Q., & Wang, F. Y. 2018, *ApJ*, **852**, 1  
 Zhang, G. Q., & Wang, F. Y. 2019, *MNRAS*, **487**, 3672  
 Zhou, B., Li, X., Wang, T., Fan, Y.-Z., & Wei, D.-M. 2014, *PhRvD*, **89**, 107303